Title

Nanocarbon Enforced Anisotropic MusCAMLR for Rapid Rescuing of Mechanically Damaged Skeletal Muscles

Introduction

Skeletal muscles as one of the major organs of the human body frequently exposed several causal events like skiing, mountaineering, road accidents, battlefield activities etc., which result in mechanical damage of the skeletal muscles. These types of injuries are associated with loss of muscle mass and destruction of structural orientation etc., which leads to functional inability of the skeletal muscles. A set of biological events include degradation of extracellular matrix (ECM), inflammation and initiation of pain production etc., become conspicuous as exaggerated responses to the muscle damage [1]. Several strategies like improving the myogenic potential of satellite cells (stem cells of skeletal muscles), enhancing the strength of remaining myofibers etc., have been taken into account to improve the treatment of such mechanically damaged muscles [2]. These approaches are found to be limited because of reduced cell migration, viability and application of immunosuppressive therapy [2,3]. Despite the absence of any correlation of between pain production and muscle damage, the nonsteroidal anti-inflammatory drugs (NSAIDs) have also been applied to reduce pain production as incase of strain induced mechanical damage to skeletal muscles [1,4]. Various established reports suggested that these NSAIDs are found to be side effect inducing and have no effect over mechanically damaged muscles [5,6]. Although significant advancements have been made towards the development of tissue engineering scaffolds to enhance the muscle cells regeneration, but these strategies are not adequate because of design of the construct, immunogenic responses from host tissue etc. Several complex tools e.g., electrospinning, 3D printing, etc., have also been utilized to maintain anisotropic well aligned morphology to support the damaged muscle fibers inside the physiological environment [7-9]. Towards this direction design and development of an engineered material composite with controlled anisotropic architecture, mechanically compatible and capable of supporting muscle tissue regeneration is always a need to circumvent these issues with conventional strategies. Our study reveals the state of the art of development and validation of application of a novel musculo-responsive polymer carbon composite (MusCAMLR) by enforcing a thermo-responsive polymer Poly (N-isopropyl acrylamide) (PNIPAM) using a selectively passivated carbon nanoparticle (CNPs). This integration of selectively passivated CNPs could

bring an anisotropic gelation pattern in PNIPAM hydrogel through tuning its gelation temperature [10,11] from ~32 °C to ~37 °C which is closer to the physiological temperature. This temperature sensitive anisotropic gelation pattern was comparable to the orientation of actin and myosin in the sarcomere which are responsible to generate unidirectional stiffening using ATP as an energy source [11,12]. We have further experimentally demonstrated the mechanical compatibility, myotube regenerating ability of MusCAMLR *in vitro.* The intramuscular injection MusCAMLR could produce complete structural recovery within 72h in a mechanically damaged skeletal muscle animal model.

Objectives

The objective of this study was to develop an anisotropic biocompatible material composite capable of providing muscle like well aligned morphology, mechanical compatibility with myotube in physiological conditions to support differentiation of muscle cells for the recovery of mechanically damaged skeletal muscles.

Material and Methods

Materials PNIPAM; average molecular weight (Mn) = ~40,000) was procured from Sigma Aldrich and sucrose (molecular weight (Mw) = 342.30; was purchased from Merck Life Science, India.

Methods

Preparation of CNP, CNP-PNIPAM, CNP+PNIPAM and MusCAMLR: A microwave assisted oxidation was carried out at 130ºC for 1h using 10%(w/v) sucrose solubilized in milli-Q water Microwave-Ultrasonic-Ultraviolet Synthesis/Extraction/Reactor System (Nu-Tech, Model: NuWav-Pro, India) for the synthesis of CNPs [13,14]. CNP co prepared with PNIPAM (CNP-PNIPAM) was synthesized by mixing 0.1% (w/v) PNIPAM in 10%(w/v) sucrose solution inside a pressure chamber of Microwave-Ultrasonic-Ultraviolet Synthesis/Extraction/Reactor System at 150°C for 45 min. CNP-PNIPAM and CNPs were mixed separately with PNIPAM at 1:4; w/w ratio in 5mL volume of milli-Q water to prepare MusCAMLR and CNP+PNIPAM.

Physicochemical characterization: CNP, CNP-PNIPAM was characterized by dynamic light scattering (DLS) Nano series Malvern Zeta sizer, measurement of zetapotential, UV-Vis spectrophotometric measurement (UV 2450, Shimadzu), Transmission electron microscopic (TEM), investigation (TEM; Technai120 KV, lanthanum hexaboride filament), fluorescence spectroscopy En Spire 2300 plate reader. MusCAMLR and CNP+PNIPAM was characterized

DLS, scanning electron microscopy (SEM) (Zeiss) investigation, TEM investigation, , FT-IR spectroscopy, X-ray diffraction (XRD) (PANalytical), raman spectroscopy (Spectra Pro 2500i) and confocal microscopy (Zeiss LSM 700).

Cell culture:

Mouse myoblast (C2C12) and mouse fibroblast (NIH/3T3) was cultured in a growth medium (GM) prepared using DMEM (Thermo Fisher Scientific) supplemented with 1% antibiotic mixture of Penicillin-Streptomycin-Neomycin (PSN) (Thermo Fisher Scientific) and 10% fetal bovine serum (FBS) inside an incubator maintained with 5% CO_2 and 37°C temperature. Cells were passaged at a regular interval using 0.05% Trypsin EDTA (Thermo Fisher Scientific). Myoblasts to myotube differentiation was carried out using a differentiation medium (DM) prepared using DMEM supplemented with (0.5-1) % FBS and PSN after cells were reached to a confluency of ~80% [15].

Confocal microscopy-based investigation: Cytoskeletal morphology was visualized by staining using Phalloidin conjugated with Alexa flour 594. Myoblasts to myotube differentiation was validated by immunocytochemistry (ICC). Cells were fixed using 4% (w/v) Paraformaldehyde and permeabilized using a buffer containing PBS and 0.2% triton X-100 and 1% BSA. Myosin heavy chain (MHC) antibody (R&D system, USA) staining was performed at 1:100 dilution at 4 °C overnight. Thereafter cells were washed and treated with secondary anti mouse antibody conjugated with Alexa flour 594 (1:1000 dilution) in room temperature for 1h. After that cells were again washed, and proceeds for slides preparation using a DAPI containing mounting media. Finally, cells were visualized under a confocal microscope (Zeiss LSM 700).

Cell-MusCAMLR interaction: The interaction of MusCAMLR with C2C12 myoblasts, myotubes and NIH/3T3 fibroblasts cells were studied under a SEM and atomic force microscope (AFM). For studying the interaction of live cells, cells were grown for 24h over a surface coated with PNIPAM, CNP+PNIPAM and MusCAMLR. The viable cell percentage was measured by MTT assay [16]. Thereafter cells were fixed placed on a copper stub and imaged under SEM. For investigating the interaction with fixed cells, cells were fixed with 4 % (w/v) paraformaldehyde and then mixed with PNIPAM, CNP+PNIPAM and MusCAMLR. Thereafter samples were placed on an aluminum foil and dried properly. Further samples were placed on copper stubs to visualize under SEM. cells grown over PNIPAM and MusCAMLR were also visualized under AFM (Oxford Instruments, Asylum Research AFM). Different surface parameters were analyzed throughout the scanned

area in an interval of 2 µm. Further, mechanical parameters were investigated using tapping mode of AFM through force mapping. A silicon nitride probe (spherical geometry with 100 nm nominal radius) (Micro Cantilever, Olympus, Japan) with resonant frequency 61.6-90.0 kHz, spring constant of 1.17-3.51 nN/nm. A satisfactory indentation depth was achieved using a ~50 nN force trigger point. The hertz model (equation 1) [10] was used to calculate the modulus elasticity from force map data.

Equation 1.

$$F = \frac{4}{3} \frac{E \sqrt{r_{tip}}}{(1 - v^2)} d^{3/2}$$

Where E is the modulus of elasticity the sample, v is indicating the Poisson's ratio, F is indicating indentation force r_{tip} is the radius of the indenter, and d is the indentation depth.

The height force profile was obtained by analyzing the height-force map through and counting the trough and crest depending on the force-height profile. AFM data were analyzed using Igor Pro (6.37, MFP3D 15.00.92) software.

In vivo study:

For conducting *in vivo* experiments, ethical approval was obtained from Institutional Animal Ethics Committee (IAEC) of IIT Kanpur. 8-10 weeks old 15 SD rats with a weight of 220-250g was procured from CSIR-Central Drug Research Institute, Lucknow, India. Animals were randomly divided into 3 groups named as healthy control group, damaged muscle group/delayed onset muscle soreness (DOMS) group and MusCAMLR treated group. Animals were exposed to a high intensity eccentric exercise protocol in a motor driven rodent treadmill (Orchid Scientific, India) at an inclination angle of -16° for 90 min with a speed of 16 m/min for the induction of muscle damage (DOMS) [17]. Blood samples were collected from all groups through retro-orbital technique at 36h and108h time point. Blood serum creatine kinase level was measured from a commercial pathology laboratory. MusCAMLR was applied through intramuscular injection of (200 mg/kg body weight) after 36h of the induction of muscle damage. After 108h of observation animals were

sacrificed and all vital organs like heart, liver, kidney, lung, intestine, spleen and triceps brachii (TB) muscles were harvested for further investigations.

Haematoxylin and eosin staining (H&E staining):

Paraffin embedded tissue blocks were prepared using a standard procedure [18]. 10 µm thick tissue sections were obtained using microtome, stained using H&E stain and visualized under a light microscope. ImageJ software was used to analyze Muscle tissue cross sectional area and percentage of centralized nuclei from the images.

Assessment of mechanical parameter of muscle tissue: Deparaffinized 10 µm thick muscle tissue sections were placed on a glass coverslip and mechanical parameters were measured using force mapping mode of AFM. A silicon probe (Oxford instruments) with resonant frequency 50-90.0 kHz, spring constant of 0.6-3.5 nN/nm. A satisfactory indentation depth was achieved using a ~3 nN force trigger point.

Assessment of sarcomeres' morphology: Deparaffinized 10 µm thick muscle tissue sections were placed on a glass coverslip. Further, the glass coverslip was placed on the copper stub and coated using gold sputtering to visualize under SEM. A secondary fixation was carried out using 1% osmium tetroxide (SRL Pvt. Ltd. India) to the glutaraldehyde fixed tissue sections for performing toluidine blue staining [19,20]. Eponate 12 resin (TED PELLA, INC.) was used for embedding the fixed tissue after treatment with ascending graded alcohol. Tissue sections with 1µm thickness were stained using Toluidine blue (Sigma Aldrich) and visualized under light microscope.

Results

A material capable of generating physiological cue responsive network similar to myotube was required for the preparation of MusCAMLR. Among various possible alternatives, a temperature responsive hydrogel was preferred which can be tuned to generate physiological temperature responsive network supportive to the damaged skeletal muscle tissue, biocompatible and a possible non-drug therapeutic alternative to the side effect inducing and less effective conventional therapies [21]. Towards this direction PNIPAM was chosen as temperature responsive hydrogel and modified using a potent, hydrophilic, and selectively passivated nanosized carbon particles to tune its gelation temperature closer to physiological temperature.

Preparation and characterization of MusCAMLR.

PNIPAM fails to provide expansion-contraction like behavior as skeletal muscles owing to its isotropic gelation at ~32 °C [10,11]. To bring this muscle anisotropic behavior in PNIPAM hydrogel incorporation of an additive was needed [22, 23]. Among many other possibilities biocompatible hydrophilic, auto fluorescent, easily preparable and capable of interacting with PNIPAM polymers nanosized carbon particles were chosen. The fluorescent property of these carbon nanoparticles (CNPs) could also make the overall system traceable through fluorescent imaging [13,14]. For further improving the interacting ability a novel nano sized system was prepared by selectively passivating the CNP surfaces with PNIPAM (CNP-PNIPAM). CNPs were prepared from sucrose as a carbon source using microwave assisted hydrothermal method while CNP-PNIPAM was prepared by the similar method inside a pressure chamber. It was observed that CNP particle was ~556± 99 nm which reduced to ~217± 63 nm in case of CNP-PNIPAM (Figure 1a) from the measurement of hydrodynamic diameter. Similarly, the zeta potential of CNP was -9 mV, while it was -5 mV in case of CNP-PNIPAM. This reduction of zeta potential is probably owing to changes in abundance of negatively charged carboxylic acid groups on the surface of nanoparticles (Figure 1a) [24]. The absorption maxima (λ_{max}) at 280 nm and at 360 nm probably because of π- π* transition and due to n- π* transition respectively was observed in the ultraviolet-Visible (*UV-Vis*) absorption spectra of CNPs. A decrease in absorption intensity at λ_{max} was visible in *Uv-Vis* absorption spectra of CNP-PNIPAM, probably because of masking of surface functionalities which are responsible for optical properties in CNPs (Figure 1b). Further, fluorescence emission spectra of CNP and CNP-PNIPAM upon excitation at their characteristic λ_{max} of 360 nm showed that the emission maxima of CNP was ~ 490 nm, which was shifted to ~ 470 nm in case of CNP-PNIPAM with a reduction in emission intensity (Figure 1c). These characteristic optical properties ensured the successful synthesis of auto-fluorescent CNP and CNP-PNIPAM, where reduced hydrodynamic diameter and surface charge were reported. From the analysis of TEM images (Figure 1d-1e) it was observed that the anhydrous diameter of CNP and CNP-PNIPAM was ~126±11 and ~26±3 nm, respectively (Figure 1i). The Composite of CNP and PNIPAM (CNP+PNIPAM) was prepared by mixing CNP (20 mg/ml) to PNIPAM (80 mg/ml) solution for tuning the gelation temperature of PNIPAM. It was found that these bare CNPs at 20 mg/ml concentration could tune the gelation temperature to 34°C and which was maintained at 37°C (Figure 1f). To achieve gelation further close to the physiological temperature another nano system CNP-PNIPAM was incorporated at 20 mg/ml concentration to the 80 mg/ml PNIPAM solution. Interestingly it was found that this combination could tune the gelation of PNIPAM to

37°C. This combination was named MusCAMLR. The DLS investigation established the reversible transition in hydrodynamic diameter in accordance with the change in temperature and the change of hydrodynamic diameter was maximum in case of MusCAMLR (Figure 1g). The TEM image of MusCAMLR revealed its nearly spherical anhydrous morphology with a diameter of ~214±13 nm (Figure 1h – 1i). Further, to evaluate the interaction of CNP and CNP-PNIPAM with PNIPAM in respective composites, a Fourier transform infrared (FT-IR) spectroscopy was performed (Figure 1j). The analysis of spectra revealed that all characteristic bands like N-H stretching, N-H bending and C=O stretching vibration etc., were present. Transmittance peaks correspond to N-H bending of amide II and C=O stretching of amide I at 1546 cm^{-1} and 1648 cm^{-1} respectively in PNIPAM were shifted to higher wavenumber of 1549 cm^{-1} and 1651 cm^{-1} in case of CNP+PNIPAM and 1554 cm^{-1} and 1651 cm^{-1} for MusCAMLR [25,26]. Similarly, transmittance peaks at 3073 cm^{-1}, 3301 cm^{-1} and 3436 cm^{-1} correspond to N-H stretching of secondary amides in PNIPAM was shifted to 3081 cm^{-1}, 3296 cm^{-1} and 3446 cm^{-1} in case of CNP+PNIPAM and 3083 cm^{-1}, 3285 cm^{-1} and 3452 cm^{-1} in case of MusCAMLR. These shifts of IR bands were presumably due to hydrogen bonding interaction between CNP and PNIPAM, which was more in MusCAMLR due to more interaction with CNP-PNIPAM. The peak at 1044 cm^{-1} in CNP+PNIPAM indicates the C-O stretching of primary alcohol present in the CNPs surface which was shifted to 1059 cm^{-1} in MusCAMLR. It was probably because of the involvement of primary alcohol group in hydrogen bonding with PNIPAM. Further the X-ray diffraction (XRD) pattern revealed the characteristic diffraction peak PNIPAM at 2θ = 7.5°, 20.5° and a small hump at 41.3°, whereas the diffraction peak of CNP-PNIPAM was observed at 2θ = 18°. However, the diffraction peak of MusCAMLR was observed at 2θ = 7.5°, 20.5° with the disappearance of the diffraction peak of CNP-PNIPAM and the small hump at 41.3°. This dictates the successful penetration of CNP-PNIPAM inside the PNIPAM polymer matrix (Figure 1k) [27]. Raman spectroscopic characterization (Figure 1l) showed a reduction in intensity in CNP+PNIPAM, which was further reduced in MusCAMLR in comparison with PNIPAM [28-30]. This implies the interaction between CNP with PNIPAM which was further enhanced MusCAMLR.
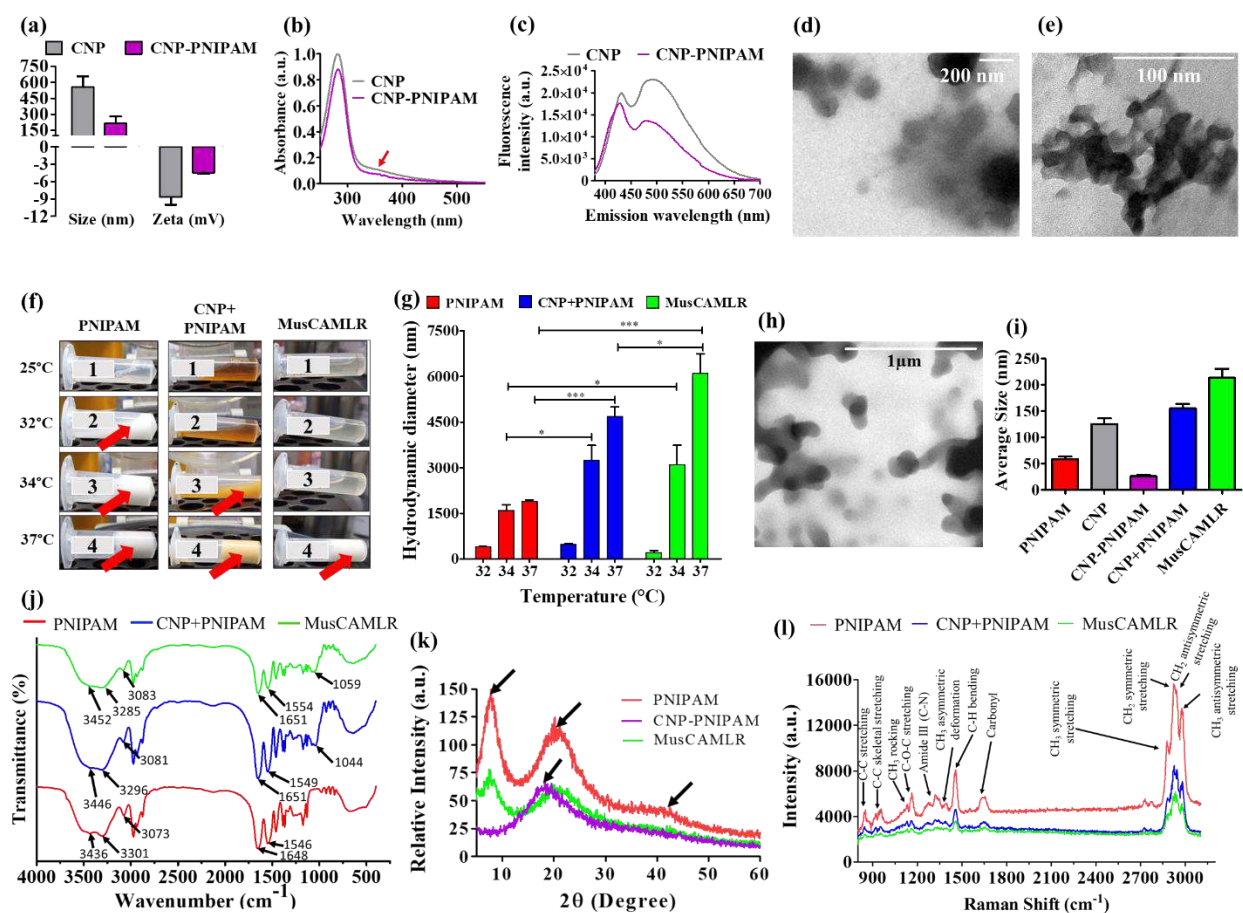
Figure 1. Physio-chemical characterization of MusCAMLR. a) Hydrodynamic diameter, and zeta potential of CNP and CNP-PNIPAM. b) *UV-Vis* absorption spectra of CNP and CNP-PNIPAM. The red arrow indicates the characteristic absorption of CNP at ~360 nm. c) Fluorescence emission spectra of CNP and CNP-PNIPAM at the excitation wavelength of 360 nm. d-e) TEM images of CNP and CNP-PNIPAM. f) Visualization of tuned gelation pattern at different temperatures. g) Temperature dependent alteration in hydrodynamic diameter of PNIPAM, CNP+PNIPAM and MusCAMLR samples. Biostatistical analysis represents *** significance with P < 0.001, * significance with P < 0.05. h) TEM image of MusCAMLR. i) Analysis of average anhydrous size of PNIPAM, CNP, CNP-PNIPAM, CNP+PNIPAM, MusCAMLR from TEM images. j) FTIR spectra of PNIPAM, CNP+PNIPAM and MusCAMLR. k) XRD patterns of PNIPAM, CNP-PNIPAM and MusCAMLR. l) Raman spectra of PNIPAM, CNP+PNIPAM and MusCAMLR.

The investigation of surface morphology revealed an uncontrolled surface arrangement of PNIPAM without any specific growth pattern. This uncontrolled surface morphology was transformed to sphere like projection over the surface after addition of CNP. Intriguingly CNP-PNIPAM incorporation produces very controlled and repetitive sandwich like structures over the surface of MusCAMLR (Figure 2a). This revealed an anisotropic surface morphology of MusCAMLR. Further temperature dependent confocal microscopic investigation using the fluorescent property of CNP-PNIPAM was performed to explore the phenomenon of anisotropic expansion in MusCAMLR. It was hypothesized that CNP-PNIPAM should orient itself according to orientation of PNIPAM matrix at 37 °C if an anisotropic expansion had to happen in the polymer network. It was observed that indeed these smartly passivated CNP-PNIPAM particles were arranged themselves in the longitudinal direction in a linear fashion (Figure 2b). This arrangement was observed after ~3 min exposure to 37 °C and it ensured the anisotropic expansion phenomenon in MusCAMLR. The representative schematic structures of MusCAMLR, CNP-PNIPAM and PNIPAM have been shown in Figure 2c based on these aforesaid characterizations.
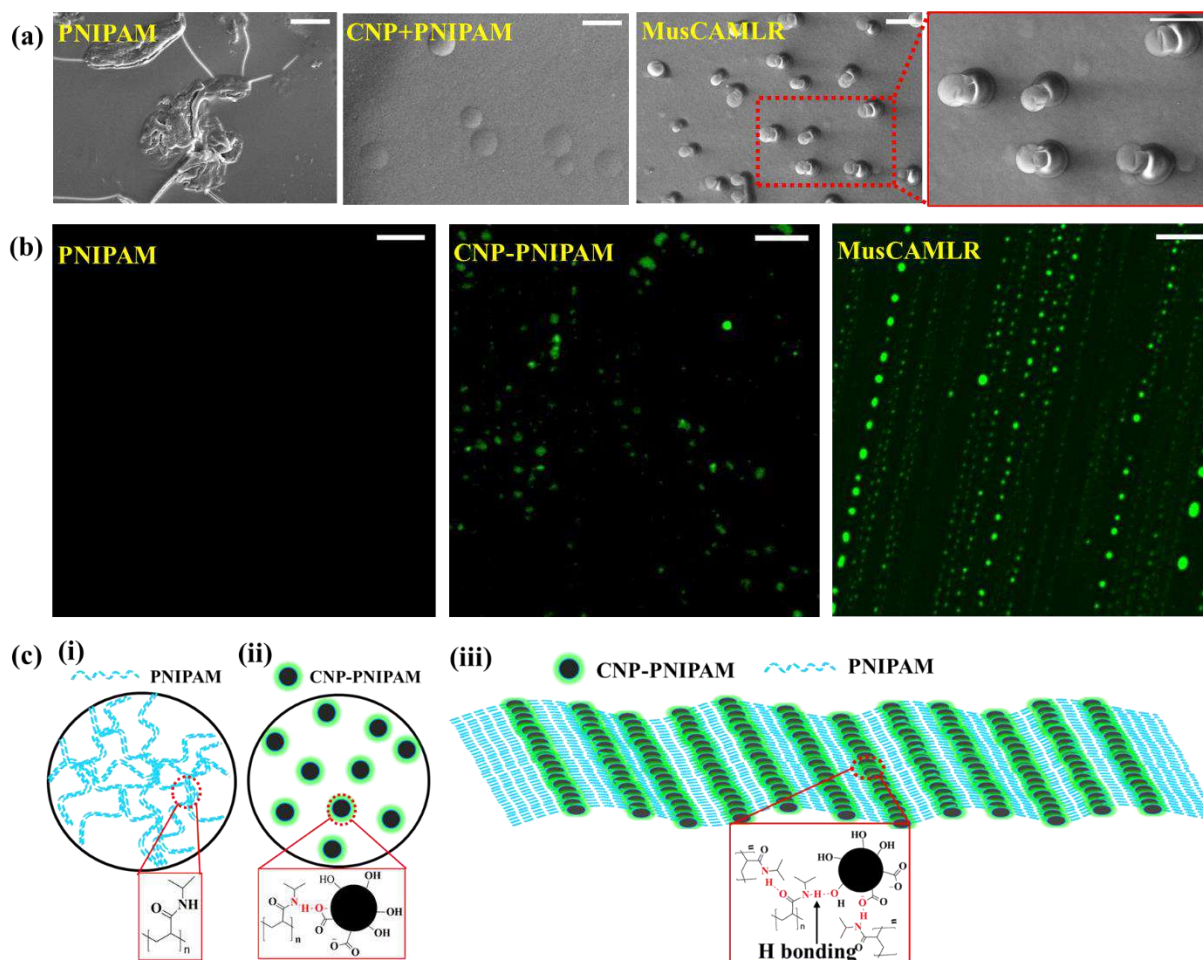
Figure 2. Structural anisotropy of MusCAMLR. a) SEM images of PNIPAM, CNP+PNIPAM and MusCAMLR. The magnified area is represented by red rectangle for further details. Scale bar = 20 μm. b) Confocal microscopic images of PNIPAM, CNP+PNIPAM and MusCAMLR obtained at 37 °C. Scale bar =10 μm. c) Schematic representation of the arrangement network of i) PNIPAM ii) CNP-PNIPAM iii) MusCAMLR. The probable arrangement of chemical entities in different samples is represented by the red dotted circle.

Evaluation of MusCAMLR's interaction with muscle cells.

SEM images were obtained in different frameworks for the visualization of the impact of interaction of muscle cells in PNIPAM, CNP+PNIPAM and MusCAMLR. In the first set of experiments, C2C12 myoblasts were cultured over a surface coated with PNIPAM, CNP+PNIPAM and MusCAMLR. Interestingly a material network structure was observed over the surface of MusCAMLR (Figure 3aiii). These structures were different than the morphology found either in PNIPAM or CNP+PNIPAM samples (Figure 3ai – 3aii). Initially it was thought that this distinguishable network like structure found over the surface of MusCAMLR as a remark of mechanical interaction of alive

and growing myoblasts. To verify this assumption, a second set of experiments were designed using prefixed C2C12 myoblast cells which were mixed with PNIPAM, CNP+PNIPAM and MusCAMLR, in different samples. Here none of the samples gave network like structures as seen in SEM investigations (Figure 3aiv – 3avi). These experiments proved the impact of mechanical interaction of live cells to change the morphology of prepared samples. A thiazolyl blue tetrazolium bromide (MTT) assay of myoblasts cells grew over PNIPAM, CNP+PNIPAM and MusCAMLR coated surface in a similar experimental condition showed the presence of a significantly higher percentage of metabolically active cells (~75%) over MusCAMLR surface with respect to either PNIPAM or CNP+PNIPAM coated surfaces (Figure 3b). This observation suggested that the special network like surface topography over the MusCAMLR surface was presumably due to the effect of mechanical interaction of proliferating myoblasts cells over the surface of MusCAMLR. Myoblasts were differentiated in a differentiation medium for 7days to myotube to further explore this interaction. This differentiated system provides resemblance to myofiber which will give enough indication about response of MusCAMLR *in vivo* [31]. Confocal microscopic investigation was performed to visualize the cytoskeletal morphology of multi nucleated myotubes by staining using Alexa flour 594-Phalloidin and expression of myosin heavy chain (MHC) by immunostaining. It was observed that the differentiated myotubes were of elongated cytoskeletal morphology (Figure 3c) and express higher MHC as perceived from comparatively intense fluorescence intensity with respect to myoblast (Figure 3d-e) [32,33]. Thereafter the myotube differentiation was carried out over MusCAMLR coated surface and changed in the morphology MusCAMLR was visualized under SEM. It was observed that MusCAMLR could again produce network like morphology (Figure 3f) with a significantly reduced diameter in compared to the diameter of the network developed in presence of myoblasts (Figure 3h)**.** The specificity of this network formation was further investigated using another control cells. NIH/3T3 mouse fibroblasts cells were preferred for this study because of their abundance as an integral resident in skeletal muscles [34]. SEM based investigations after growing NIH/3T3 cells over a MusCAMLR coated surface showed the formation of no such network structures (Figure 3g). This study ensured the peculiarity and specificity of the network to the muscle cells both in myoblasts and myotube state. Further AFM based imaging (Figure 4a –d) and analysis of surface profile revealed the similarity of the average intra trough distance of the myotube surface differentiated over MusCAMLR to control myotubes differentiated over regular cell culture plate surfaces (Figure 4e). This is to note that

NIH/3T3 grown over MusCAMLR surface or myotube differentiated over PNIPAM surface were not of any significant similarity to the control myotube or myotube differentiated over MusCAMLR.
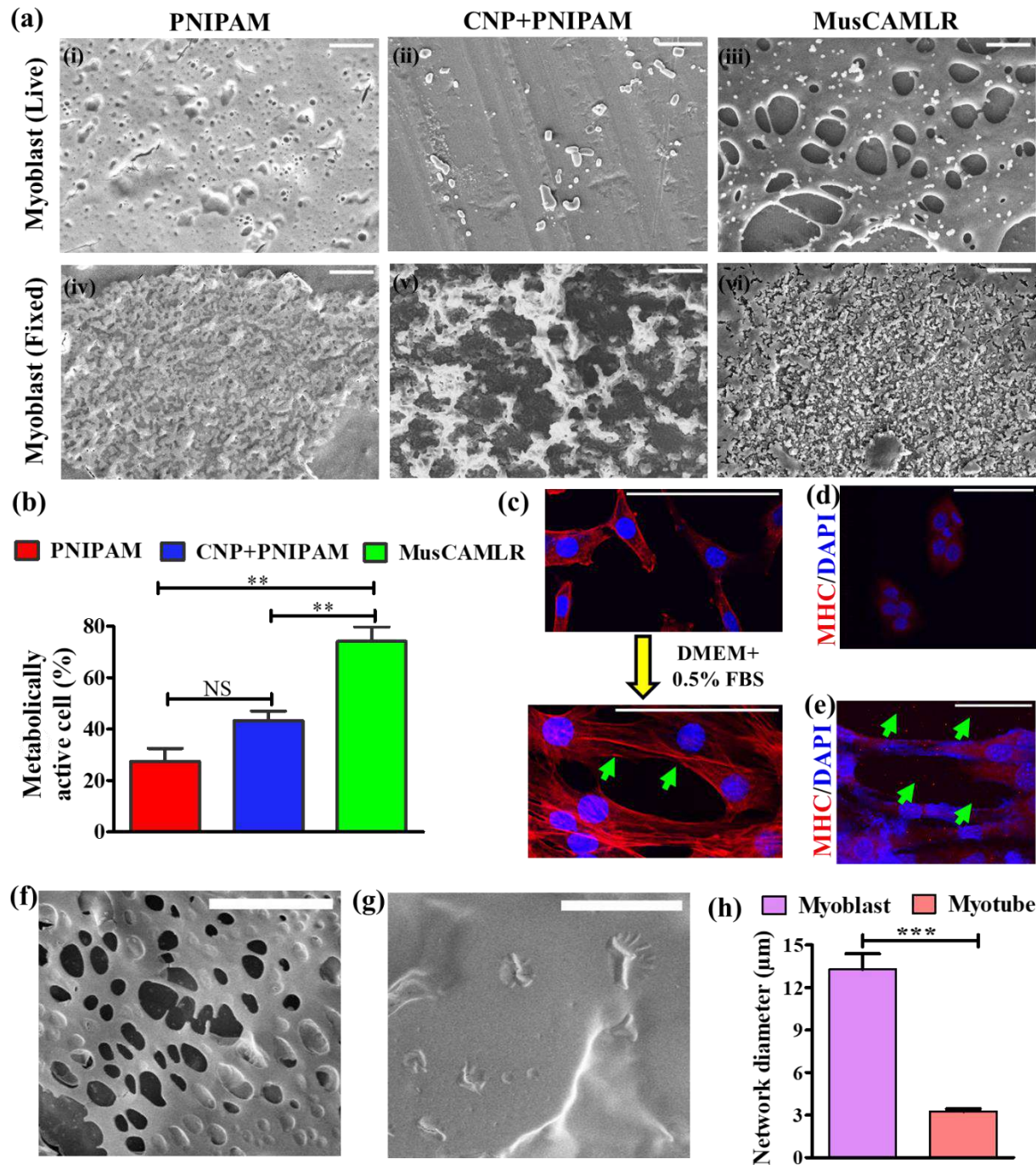
Figure 3. Interaction study between MusCAMLR and muscle cells. a) SEM images of (i) PNIPAM, (ii) CNP+PNIPAM and (iii) MusCAMLR in interaction with live myoblast cells, SEM images of (iv) PNIPAM, (v) CNP+PNIPAM and (vi) MusCAMLR in interaction with fixed myoblast cells. Scale bar = 20 µm. b) Measurement of metabolically active cells present in interaction with different samples. Biostatistical analysis represents ** = significance with $p < 0.001$ and NS = Not significant. c) Myoblast to myotube differentiation as imaged by staining with Alexa flour 594-Phalloidin. Scale bar =100 µm. MHC-stained images of d) myoblast and e) myotube under confocal microscope. Scale bar in d & e =100 µm. f) SEM images of MusCAMLR interaction with myotube. Scale bar = 20µm. g) SEM images of MusCAMLR interaction with NIH/3T3 cell line. Scale bar = 20 µm. h) Quantification of network diameter in MusCAMLR produced after interaction with myoblasts and myotube. Biostatistical analysis represents *** = significance with $p < 0.0001$.
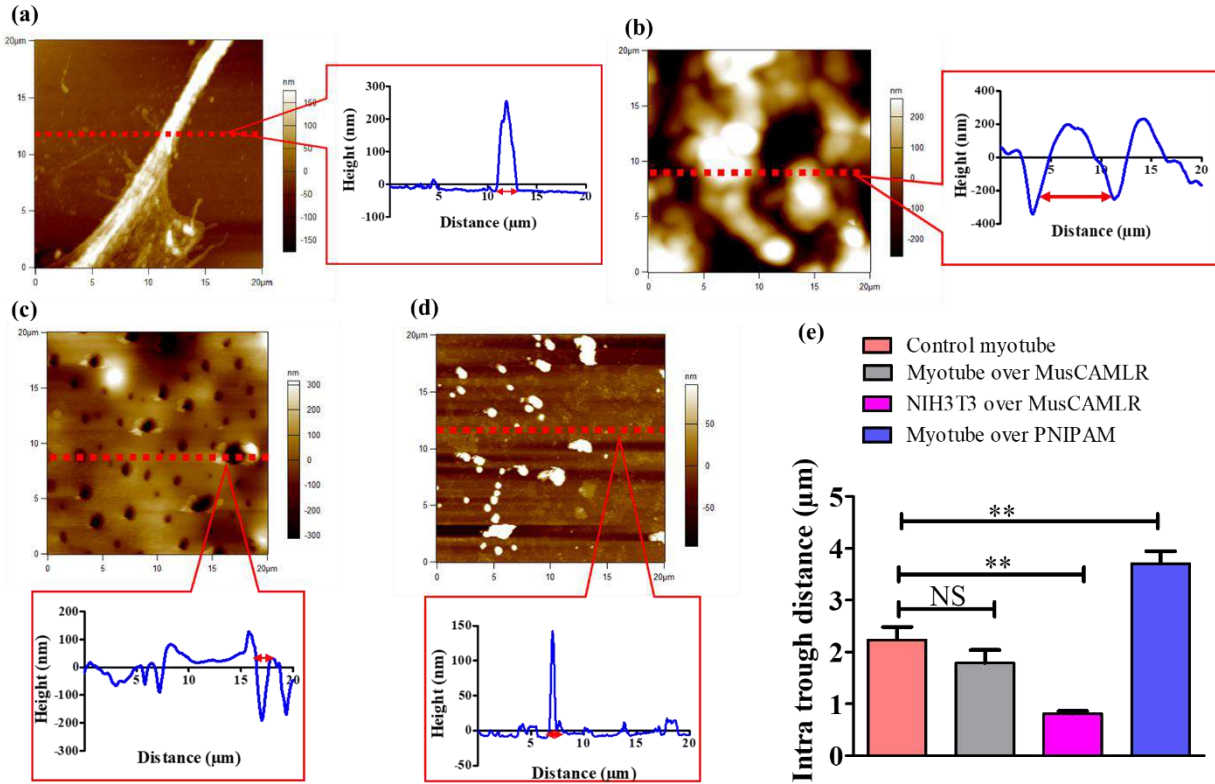
Figure 4. AFM images and its analyzed representative surface profile plot of a) control myotube, b) interaction between PNIPAM and myotube, c) interaction between MusCAMLR and myotube, and d) interaction between MusCAMLR and NIH/3T3 cells. Double headed red arrow indicating the intra trough distance in the surface profile plot in the image (a-d). e) Quantification of intra trough distance from analysis of surface profile in (a-d). Biostatistical analysis represents ** = significance with $p < 0.001$ and NS= Not significant.

Mechanical similarity and myoblast differentiation ability of MusCAMLR.

In general, structural, and functional similarity with biologically concerned tissue determines the success of a material developed for biological application. Here the mechanical similarity of MusCAMLR with skeletal muscle tissue would be required to make it suitable for interaction in a similar biological scenario. The force mapping analysis revealed that modulus of elasticity was significantly low in case of MusCAMLR and further reduced when myoblasts were grown over MusCAMLR, in comparison to PNIPAM (Figure 5a-5b). However, the modulus of elasticity of myotube differentiated over MusCAMLR was similar as control myotubes, while it was significantly different than the modulus of elasticity of myoblasts (Figure 5c). This study disclosed the excellent mechanical compatibility of myotube differentiated over the surface of MusCAMLR. The analysis of force height map of MusCAMLR (Figure 5d-e), PNIPAM, myoblast grown over MusCAMLR, myotube grown over MusCAMLR, and control myoblasts (data not shown) interpreted that the average number of ridges over the surface of MusCAMLR was similar to the myotube grown over MusCAMLR and control myotubes (Figure 5f). This ensured high complementarity of the material for its functioning owing to the similar order of spatial range of forces. Further, differentiation ability of myoblasts was investigated over the surface of MusCAMLR by visualizing cytoskeletal morphology and quantifying fusion index as a measure of extent for the myotube differentiation. Alexa flour 594-Phalloidin stained confocal microscopic images revealed that myotubes differentiation over the surface of MusCAMLR (Figure 5h) were with a properly elongated cytoskeletal morphology than the myotube differentiated over the surface of PNIPAM (Figure 5g). Further, immunocytochemical investigation showed the generation of multinucleated tube with higher level of expression of MHC over MusCAMLR (Figure 5i) in comparison to PNIPAM (data not shown). Analysis of Giemsa-stained light microscopic images revealed that myotube differentiated over the surface of MusCAMLR had very high fusion index, which was comparable to values from control myotube, whereas myotube differentiated over PNIPAM surface had significantly lower fusion index. It could be inferred that MusCAMLR is capable of maintaining the differentiation of myoblast *in vitro* (Figure 5j).
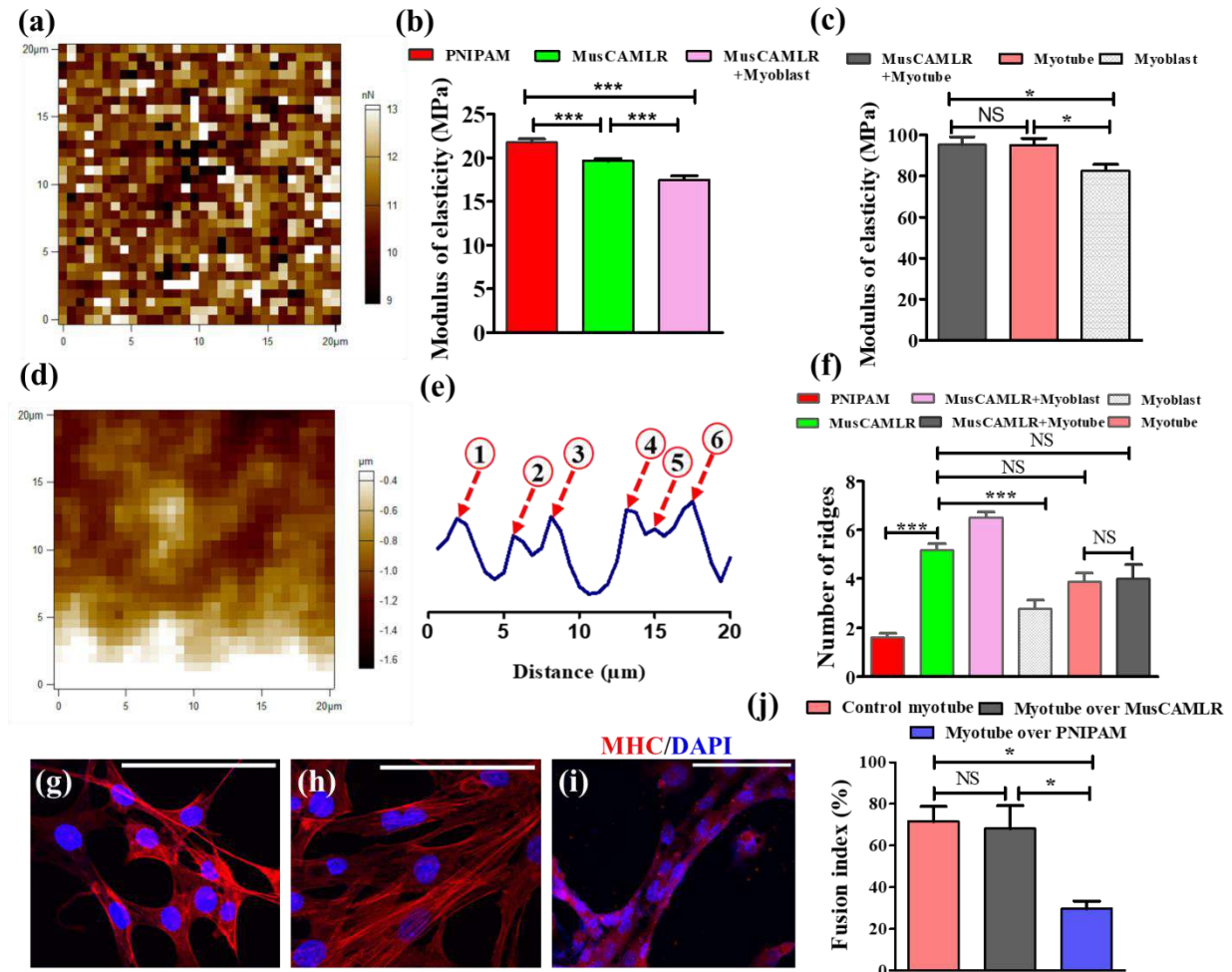
Figure 5. Quantification of mechanical parameters and differentiation ability of muscle cells over the surface of MusCAMLR. a) Force map of MusCAMLR from AFM investigation. b) Modulus of elasticity of PNIPAM, MusCAMLR and myoblast grown over MusCAMLR (MusCAMLR + Myoblast) quantified from AFM force map. Biostatistical analysis represents *** = significance with p < 0.0001. c) Modulus of elasticity of myotube grown over MusCAMLR (MusCAMLR + Myotube), myotube and myoblast alone quantified from AFM force map. Biostatistical analysis represents * = significance with p < 0.01 and NS= Not Significant. d) Force-height map of MusCAMLR. e) Representative surface force height profile of MusCAMLR. Red arrows are indicating the number of ridges over the surface of the material. f) Quantification of average number ridges from the surface force height profile of PNIPAM, MusCAMLR, MusCAMLR+ myoblast, MusCAMLR+ myotube, control myoblast and control myotube. Biostatistical analysis represents *** =

significance with p < 0.0001 and NS= Not Significant. g) Alexa flour 594-Phalloidin stained confocal microscopic images of myotube over the surface PNIPAM, h) MusCAMLR. Scale bar in g and h = 100 μm. i) Immuno-stained confocal microscopic image of myotube differentiated over MusCAMLR using antibody against MHC. Scale bar =100 μm. j) Quantification of fusion index. Biostatistical analysis represents *= significance with p < 0.01 and NS= Not Significant.

In vivo Application of MusCAMLR on mechanically damaged skeletal muscles in developed animal model.

A delayed onset muscle soreness (DOMS) animal model was developed using eccentric exercise as a mechanical stimulus for examining the role of MusCAMLR to rescue mechanically damaged skeletal muscles [35]. Eccentric exercise causes strain injuries to the skeletal muscles because of the lengthening of muscle fibers. This leads to the damage of contractile elements of muscle fibers, immune response activations, leakage of muscle proteins in plasma and reduction of muscle performance [19, 36]. Measurement of serum creatine kinase (CK) level, analysis of other tissue parameters was carried out as per timeline represented in Figure 6a. A significant increment of serum CK level was noticeable at 36h after the induction of muscle damage in group 2 (DOMS group) and group 3 (MusCAMLR treated group) before the application of MusCAMLR (Figure 6b). An intramuscular injection of MusCAMLR in triceps brachii (TB) muscle resulted in recovery of serum CK levels within 72h of application i.e., at time point of 108h (Figure 6c). After these observational time points, animals were sacrificed, TB muscles and different vital organs including heart, liver, lung, kidney, spleen, and intestine were isolated. Hematoxylin & eosin (H&E) stained images of different vital organs (heart, liver, lung, kidney, spleen, intestine) suggested no significant sign of toxicity, immune activation, other adverse effects of the tissues were noted (Figure 6d-i). A similar observation was also prominent from H&E-stained images of vital organs from DOMS and healthy groups of animals (data not shown). This confirmed the noticeable biocompatible nature of MusCAMLR. The force mapping analysis data from muscle tissues of healthy, DOMS and MusCAMLR treated animal groups (Figure 6j – 6l) showed a significant increase in tissue hardness in TB muscle of DOMS group [37], which was reduced to normal level within 72h after treatment of MusCAMLR (Figure 6m).
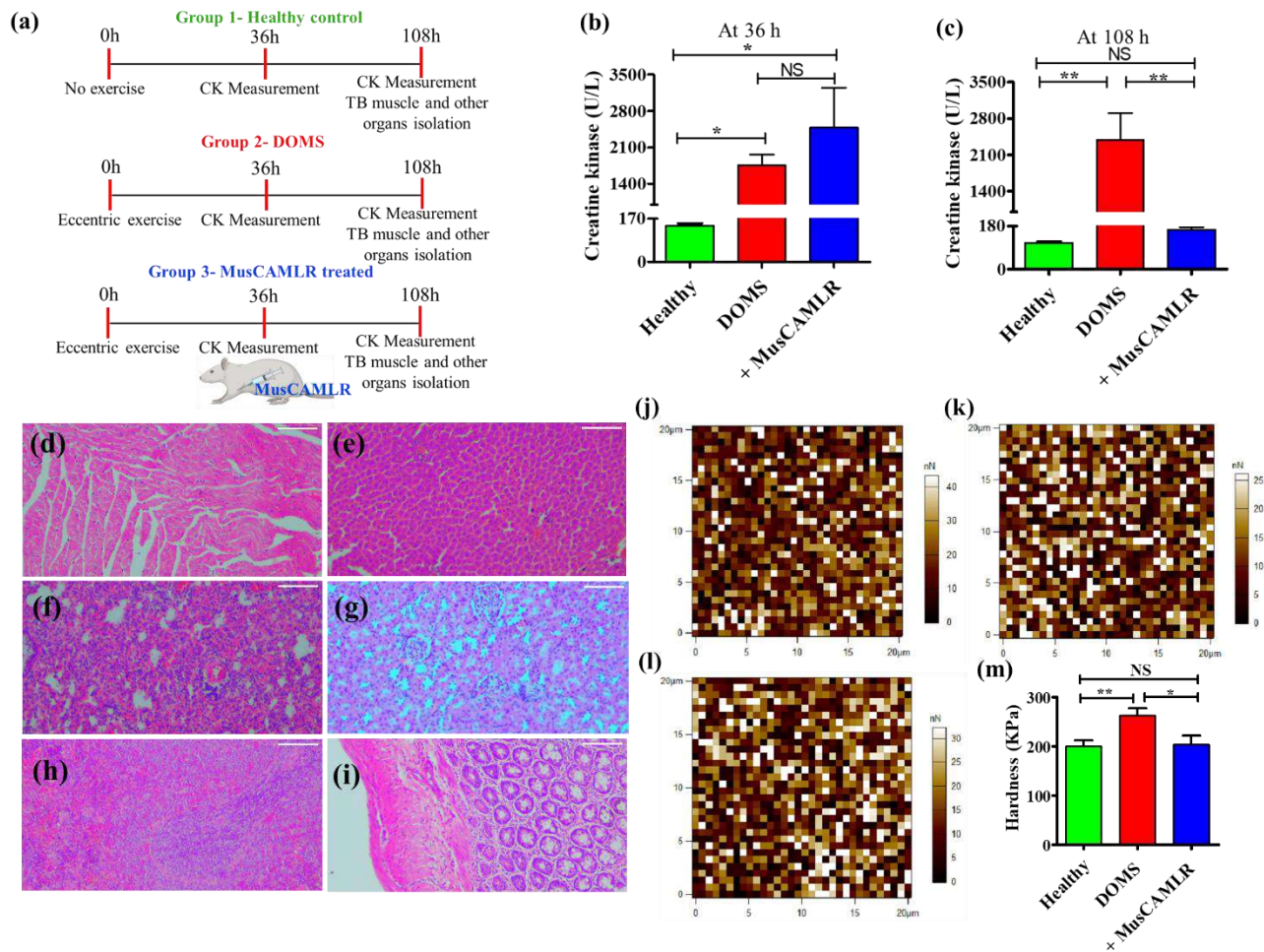
Figure 6. Application of MusCAMLR in in vivo on mechanically damaged skeletal muscle animal model. a) Schematic representation of timeline for the induction of muscle damage using eccentric exercise, measurement of CK, MusCAMLR treatment and isolation of organs from animals of three different groups. b) Level of serum creatine kinase at 36 h (before application of MusCAMLR) and c), at 108h (i.e., 72 h after application of MusCAMLR). Biostatistical analysis represents ** = significance with p < 0.002, * = significance with p < 0.01 and NS= Not Significant. d) H&E-stained light microscopic images of heart, e) liver, f) lung g) kidney h) spleen i) intestine. Scale bar in (d-e) = 100 μm. j) AFM based force map of muscle tissue from healthy, k) DOMS and l) MusCAMLR treated animals. m) Measurement of tissue hardness from the force maps of healthy, DOMS and MusCAMLR treated animals. Biostatistical analysis represents ** = significance with p < 0.01, *= significance with p < 0.05 and NS= Not Significant.

Recovery of structural integrity of skeletal muscle.

The ability of MusCAMLR to recover the structural parameters in mechanically damaged muscles was evaluated from both cross-sections as well as longitudinal sections of TB muscles. The H&E-stained images (Figure 7a -c) of muscle cross section showed that cross sectional area (Figure 7d) and the percentage of centralized nuclei (Figure 7e) was decreased significantly in damaged muscle of DOMS group. This could be interpreted as the induced atrophy [38] of the damaged muscle which was rescued after application of MusCAMLR. The further evaluation of Z line streaming was performed by different histological staining like toluidine blue staining, H&E-staining and electron microscopic investigation from the longitudinal section of TB muscle. Toluidine blue stained images showed very diffused and disrupted boundaries of sarcomere in mechanically damaged TB muscle from DOMS group suggesting the Z-disk disruption [19] in comparison to the distinct and demarcated boundaries of sarcomere in muscles from healthy group (Figure 7f -7g). The recovery of prominent demarcated boundaries of sarcomere after MusCAMLR treatment indicated the rescuing of structural integrity of TB muscles (Figure 7h). The H&E-stained images of the longitudinal section of skeletal muscle also provided similar indications of disruption of arrangement of sarcomere in the muscle from DOMS group, possibly because of streaming of Z line. The arrangement of sarcomere was rescued after MusCAMLR treatment (Figure 8a-c). Similar observation was also obtained from SEM (Figure 8d-e) and TEM investigations (data not shown).
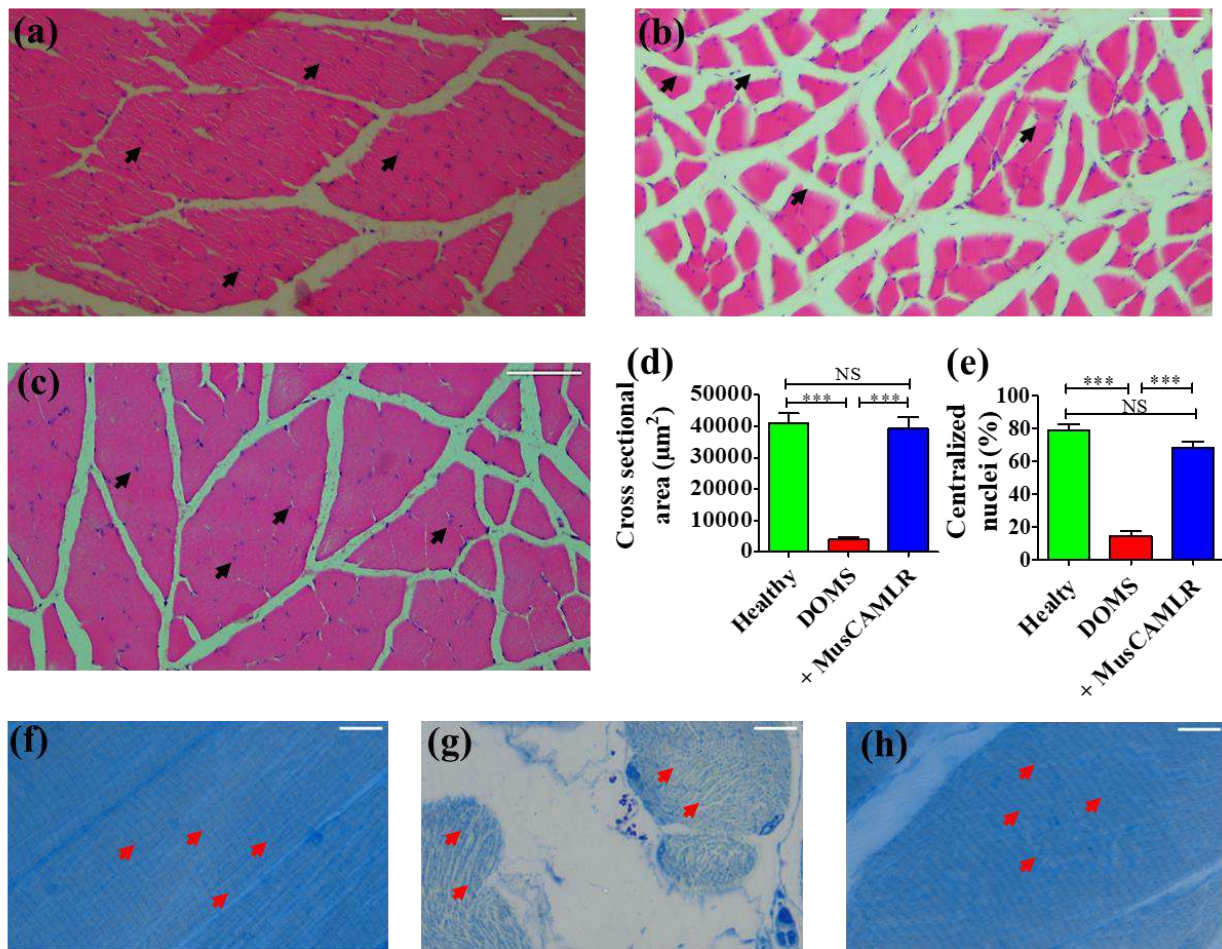
Figure 7. Recovery of structural parameters of skeletal muscles after MusCAMLR treatment. Representative H&E-stained light microscopic images of cross section of TB muscle from a) healthy, b) DOMS and c) MusCAMLR treated animals. Scale bar in (a – c) = 100 μm. Black arrows indicate the position of nuclei. d) Quantification of cross-sectional area from the cross sections of TB muscle. e) Quantification of the centralized nuclei (%) from the TB muscle cross sections. f) Toluidine blue-stained light microscopic images of longitudinal sections of TB muscle from healthy, g) DOMS, h) MusCAMLR treated group. Scale bar in (f – h) = 10 μm. Red arrows indicate the boundary of sarcomere. Biostatistical analysis represents ***= significance with p < 0.0001 and NS = Not Significant.
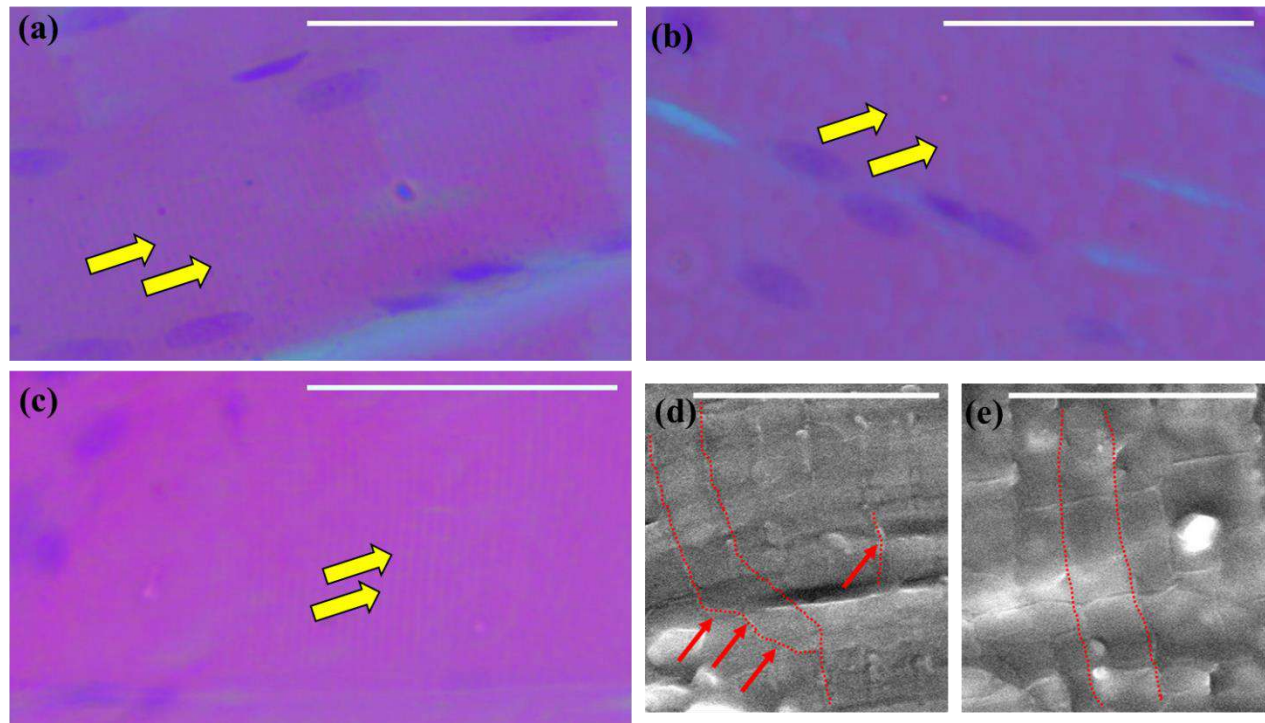
Figure 8. Sarcomere's arrangement in longitudinal section of skeletal muscle. H&E-stained light microscopic images of longitudinal section of skeletal muscle from a) healthy group, b) DOMS group and c) MusCAMLR treated group. Yellow arrows (a-c) are indicating the demarcation of sarcomere's lining and scale bar = 50 μm. Representative SEM images of sarcomere from the longitudinal section of skeletal muscles of d) DOMS and e) MusCAMLR treated group. Red line (d-e) represents demarcation of sarcomere, red arrows indicate diffused structure of Z line and scale bar = 20 μm.

Statistical Analysis

Two-way ANOVA with Bonferroni post-test was applied to compare the difference between more than two groups with more than one parameter. One way ANOVA followed by Tukey's multiple comparison test was applied to compare the significance difference between more than two groups with one parameter. The two-tailed Student's t-tests were appplied to compare the significance difference between two groups. Data were represented with mean ±SEM wherever applicable. Statistical analysis was performed in GraphPad PRISM software (Version 5.01).

Discussion

This study is a manifestation of an effort to develop non-drug therapeutic MusCAMLR by modulating the isotropic gelation behavior of PNIPAM hydrogel using smartly passivated CNP-PNIPAM. This enforcement allows the hydrogel to attain the anisotropic orientation of skeletal muscles. The preparation strategy of MusCAMLR didn't require any complex tools like chemical conjugation, thermally induced phase separation and 3D printing etc., [12,39] which brought wonderful ease to the system. This will help in translating the MusCAMLR by reducing the batch-to-batch variation. The maximum reversible expansion-contraction of hydrodynamic diameter, well aligned orientation of MusCAMLR at physiological temperature and sandwich like surface morphology dictates the influence of CNP-PNIPAM to control the material morphology. The remarkable transition of material surface topography from sandwich like structures to a special material network in presence of higher number of viable muscle cells was presumably because of transmission of forces during different cellular processes like transcellular adhesion, cytoskeletal organization etc., [40]. The similarity of force height profile of MusCAMLR with myotube and dissimilarity with myoblasts from AFM force mapping investigation indicated the more suitability of mechanical interaction between MusCAMLR and myotube. This could also be correlated to the formation of material network with different diameter in case of growing myoblasts and myotube. Excellent compatibility of mechanical parameters of MusCAMLR, ability to support the myotube differentiation with well elongated cytoskeletal morphology was only possible due to the anisotropic characteristic of MusCAMLR. Here the purpose of development of mechanically damaged DOMS model using eccentric exercise without using any drugs, snake venom like cardiotoxin etc., was to mimic real-life scenario [41-43]. The TB muscle was preferred for the intramuscular injection of MusCAMLR because of being an extensor muscle which showed muscle damage to a greater extent [44]. Recovery of biochemical (serum CK level), structural (muscle cross sectional are, arrangement of sarcomere) and mechanical parameters (tissue

hardness) by various investigations within 72h proved the possible potential of MusCAMLR to rescue the persons with higher extent of mechanical damage as incase of athletes, defense personnel etc. This study also gives proof of concept for the development of non-drug therapeutic alternatives by careful tuning of the materials' property. We didn't find any suitable gold standard treatment control in the present study after considering the mechanism of action and potency of the conventional treatment strategies like application of electric stimulation, ultrasound therapy, cryotherapy, and anti-inflammatory drugs especially NSAIDs [46]. We believe the use of any conventional used interventions would most likely be not useful to compare the recovery of structural parameters of damaged skeletal muscles [5,6,47,48]. Though some other gold standard treatment controls will be used in our future study to compare the recovery of functional parameters of damaged skeletal muscles.

Impact of the research in the advancement of knowledge or benefit to mankind

This successful translation of MusCAMLR will be beneficial for the individuals frequently exposed to mechanical injury like athletes and defense personnels etc. This will help to provide them with quick muscle recovery to reduce the loss of their active work hours and reduce financial loss to the associated organizations. Further improvements and more validations of the applications of MusCAMLR will help to develop non-drug therapeutics for other skeletal muscle damages as happens in case of muscular dystrophy, sarcopenia, and cancer cachexia etc.

Literature references

1. Stauber, W. T.; Clarkson, P. M.; Fritz, V. K.; Evans, W. J. Extracellular Matrix Disruption and Pain after Eccentric Muscle Action. *J. Appl. Physiol.* 1990, *69*, 868−874.

2. Dziki, J.; Badylak, S.; Yabroudi, M.; Sicari, B.; Ambrosio, F.; Stearns, K.; Turner, N.; Wyse, A.; Boninger, M. L.; Brown, E. H. P.; Rubin, J. P. An Acellular Biologic Scaffold Treatment for Volumetric Muscle Loss: Results of a 13-Patient Cohort Study. *npj Regener. Med.*2016, *1*, No. 16008.

3. Skuk, D.; Roy, B.; Goulet, M.; Chapdelaine, P.; Bouchard, J.-P.; Roy, R.; Dugre, F. J.; Lachance, J.-G.; Deschênes, L.; Senay, H.; Sylvain, M.; Tremblay, J. P. Dystrophin Expression in Myofibers of Duchenne Muscular Dystrophy Patients Following Intramuscular Injections of Normal Myogenic Cells. *Mol. Ther.* 2004, *9*, 475−482.

4. Cheung, K.; Hume, P. A.; Maxwell, L. Delayed Onset Muscle Soreness. *Sports Med.* 2003, *33*, 145−164.

5. Donnelly, A. E.; McCormick, K.; Maughan, R. J.; Whiting, P.H.; Clarkson, P. M. Effects of a Non-Steroidal Anti-Inflammatory Drug on Delayed Onset Muscle Soreness and Indices of Damage. *Br.J. Sports Med.* 1988, *22*, 35−38.

6. Nieman, D. C.; Dumke, C. L.; Henson, D. A.; McAnulty, S. R.; Gross, S. J.; Lind, R. H. Muscle Damage Is Linked to Cytokine Changes Following a 160-Km Race. *Brain, Behav., Immun.* 2005, *19*, 398−403.

7. Kim, J. H.; Seol, Y.-J.; Ko, I. K.; Kang, H.-W.; Lee, Y. K.; Yoo, J.J.; Atala, A.; Lee, S. J. 3D Bioprinted Human Skeletal Muscle Constructs for Muscle Function Restoration. *Sci. Rep.* 2018, *8*, No. 12307.

8. Brazile, B.; Lin, S.; Copeland, K.; Butler, J.; Cooley, J.;Brinkman-Ferguson, E.; Guan, J.; Liao, J. Ultrastructure and Biomechanics of Skeletal Muscle ECM: Implications in Tissue Regeneration. In *Bio-Instructive Scaffolds for Musculoskeletal Tissue Engineering and Regenerative Medicine*; Elsevier, 2017; pp 139−160.

9. Smoak, M. M.; Mikos, A. G. Advances in Biomaterials for Skeletal Muscle Engineering and Obstacles Still to Overcome. *Mater. Today Bio* 2020, *7*, No. 100069.

10. Schmidt, S.; Zeiser, M.; Hellweg, T.; Duschl, C.; Fery, A.; Mohwald, H. Adhesion and Mechanical Properties of PNIPAM Microgel Films and Their Potential Use as Switchable Cell Culture Substrates. *Adv. Funct. Mater.* 2010, *20*, 3235−3243.

11. de Almeida, P.; Jaspers, M.; Vaessen, S.; Tagit, O.; Portale, G.; Rowan, A. E.; Kouwer, P. H. J. Cytoskeletal Stiffening in Synthetic Hydrogels. *Nat. Commun.* 2019, *10*, No. 609.

12. Haque, M. A.; Kamita, G.; Kurokawa, T.; Tsujii, K.; Gong, J. P. Unidirectional Alignment of Lamellar Bilayer in Hydrogel: One-Dimensional Swelling, Anisotropic Modulus, and Stress/Strain Tunable Structural Color. *Adv. Mater.* 2010, *22*, 5110−5114.

13. Kundu, S.; Chatterjee, N.; Chakraborty, S.; Gupta, A.; Goswami, D.; Misra, S. K. Poly-Lysinated Nanoscale Carbon Probe for Low Power Two-Photon Bioimaging. *Spectrochim. Acta, Part A* 2022, *270*, No. 120778.

14. Chatterjee, N.; Kumar, P.; Kumar, K.; Misra, S. K. What Makes Carbon Nanoparticle a Potent Material for Biological Application? *WIREs Nanomed. Nanobiotechnol.* 2022, *14*, No. e1782.

15. Rashid, M. M.; Runci, A.; Polletta, L.; Carnevale, I.; Morgante, E.; Foglio, E.; Arcangeli, T.; Sansone, L.; Russo, M. A.; Tafani, M. Muscle LIM Protein/CSRP3: A Mechanosensor with a Role in Autophagy. *Cell Death Discovery* 2015, *1*, No. 15014.

16. Misra, S. K.; Ohoka, A.; Kolmodin, N. J.; Pan, D. Next Generation Carbon Nanoparticles for Efficient Gene Therapy. *Mo. Pharmaceutics* 2015, *12*, 375−385.

17. Armstrong, R. B.; Ogilvie, R. W.; Schwane, J. A. Eccentric Exercise-Induced Injury to Rat Skeletal Muscle. *J. Appl. Physiol.* 1983,*54*, 80−93.

18. Misra, S. K.; Ye, M.; Ostadhossein, F.; Pan, D. Pro-Haloacetate Nanoparticles for Efficient Cancer Therapy via Pyruvate Dehydrogenase Kinase Modulation. *Sci. Rep.* 2016, *6*, No. 28196.

19. Stupka, N.; Lowther, S.; Chorneyko, K.; Bourgeois, J. M.; Hogben, C.; Tarnopolsky, M. A. Gender Differences in Muscle Inflammation after Eccentric Exercise. *J. Appl. Physiol.* 2000, *89*, 2325−2332.

20. Ghnenis, A. B.; Czaikowski, R. E.; Zhang, Z. J.; Bushman, J. S.Toluidine Blue Staining of Resin-Embedded Sections for Evaluation of Peripheral Nerve Morphology. *J. Visualized Exp.* 2018, No. 58031.

21. Volpi, M.; Paradiso, A.; Costantini, M.; Świȩszkowski, W. Hydrogel-Based Fiber Biofabrication Techniques for Skeletal Muscle Tissue Engineering. *ACS Biomater. Sci. Eng.* 2022, *8*, 379−405.

22. Jain, K.; Vedarajan, R.; Watanabe, M.; Ishikiriyama, M.; Matsumi, N. Tunable LCST Behavior of Poly (N-Isopropylacrylamide/ Ionic Liquid) Copolymers. *Polym. Chem.* 2015, *6*, 6819−6825.

23. Gupta, S.; Singh, A.; Matsumi, N. Controlled Phase Behavior of Thermally Sensitive Poly(N-Isopropylacrylamide/Ionic Liquid) with Embedded Au Nanoparticles. *ACS Omega* 2019, *4*, 20923 −20930.

24. Misra, S. K.; Srivastava, I.; Tripathi, I.; Daza, E.; Ostadhossein, F.; Pan, D. Macromolecularly "Caged" Carbon Nanoparticles for Intracellular Trafficking via Switchable Photoluminescence. *J. Am. Chem. Soc.* 2017, *139*, 1746–1749.

25. Evanghelidis, A.; Beregoi, M.; Diculescu, V. C.; Galatanu, A.; Ganea, P.; Enculescu, I. Flexible Delivery Patch Systems Based on Thermoresponsive Hydrogels and Submicronic Fiber Heaters. *Sci. Rep.* 2018, *8*, No. 17555.

26. Shi, Y.; Ma, C.; Peng, L.; Yu, G. Conductive "Smart" Hybrid Hydrogels with PNIPAM and Nanostructured Conductive Polymers. *Adv. Funct. Mater.* 2015, *25*, 1219–1225.

27. Zhu, C.-H.; Lu, Y.; Peng, J.; Chen, J.-F.; Yu, S.-H. Photothermally Sensitive Poly(N-Isopropylacrylamide)/Graphene Oxide Nanocomposite Hydrogels as Remote Light-Controlled Liquid Microvalves. *Adv. Funct. Mater.* 2012, *22*, 4017–4022.

28. Sanz, B.; von Bilderling, C.; Tuninetti, J. S.; Pietrasanta, L.; Mijangos, C.; Longo, G. S.; Azzaroni, O.; Giussi, J. M. Thermally- Induced Softening of PNIPAm-Based Nanopillar Arrays. *Soft Matter* 2017, *13*, 2453–2464.

29. Nigro, V.; Ripanti, F.; Angelini, R.; Sarra, A.; Bertoldo, M.; Buratti, E.; Postorino, P.; Ruzicka, B. Molecular Mechanisms Driving the Microgels Behaviour: A Raman Spectroscopy and Dynamic Light Scattering Study. *J. Mol. Liq.* 2019, *284*, 718–724.

30. Gartia, M. R.; Misra, S. K.; Ye, M.; Schwartz-Duval, A.; Plucinski, L.; Zhou, X.; Kellner, D.; Labriola, L. T.; Pan, D. Point-of- Service, Quantitative Analysis of Ascorbic Acid in Aqueous Humor for Evaluating Anterior Globe Integrity. *Sci. Rep.* 2015, *5*, No. 16011.

31. Hupkes, M.; Jonsson, M. K. B.; Scheenen, W. J.; Rotterdam, W.; Sotoca, A. M.; Someren, E. P.; Heyden, M. A. G.; Veen, T. A.; Os, R. I. R.; Bauerschmidt, S.; Piek, E.; Ypey, D. L.; Zoelen, E. J.; Dechering, K. J. Epigenetics: DNA Demethylation Promotes Skeletal Myotube Maturation. *FASEB J.* 2011, *25*, 3861–3872.

32. White, J.; Barro, M. V.; Makarenkova, H. P.; Sanger, J. W.; Sanger, J. M. Localization of Sarcomeric Proteins During Myofibril Assembly in Cultured Mouse Primary Skeletal Myotubes. *Anat. Rec.* 2014, *297*, 1571–1584.

33. Ku, S. H.; Park, C. B. Myoblast Differentiation on Graphene Oxide. *Biomaterials* 2013, *34*, 2017−2023.

34. Chapman, M. A.; Meza, R.; Lieber, R. L. Skeletal Muscle Fibroblasts in Health and Disease. *Differentiation* 2016, *92*, 108−115.

35. Armstrong, R. B.; Ogilvie, R. W.; Schwane, J. A. Eccentric Exercise-Induced Injury to Rat Skeletal Muscle. *J. Appl. Physiol.* 1983, *54*, 80−93.

36. Garrett, W. E. Muscle Strain Injuries. *Am. J. Sports Med.* 1996,*24*, S2−S8.

37. Yanagisawa, O.; Sakuma, J.; Kawakami, Y.; Suzuki, K.; Fukubayashi, T. Effect of Exercise-Induced Muscle Damage on Muscle Hardness Evaluated by Ultrasound Real-Time Tissue Elastography. *SpringerPlus* 2015, *4*, No. 308.

38. Swist, S.; Unger, A.; Li, Y.; Voge, A.; von Frieling-Salewsky, M.; Skarlen, A.; Cacciani, N.; Braun, T.; Larsson, L.; Linke, W. A. Maintenance of Sarcomeric Integrity in Adult Muscle Cells Crucially Depends on Z-Disc Anchored Titin. *Nat. Commun.* 2020, *11*, No. 4479.

39. Jana, S.; Levengood, S. K. L.; Zhang, M. Anisotropic Materials for Skeletal-Muscle-Tissue Engineering. *Adv. Mater.* 2016, *28*, 10588−10612.

40. Discher, D. E.; Janmey, P.; Wang, Y. Tissue Cells Feel and Respond to the Stiffness of Their Substrate. *Science* 2005, *310*, 1139−1143.

41. Guardiola, O.; Andolfi, G.; Tirone, M.; Iavarone, F.; Brunelli, S.; Minchiotti, G. Induction of Acute Skeletal Muscle Regeneration by Cardiotoxin Injection. *J. Visualized Exp.* 2017, No. e54515.

42. Harris, J. B.; MacDonell, C. A. Phospholipase A2 Activity of Notexin and Its Role in Muscle Damage. *Toxicon* 1981, *19*, 419−430.

43. Plant, D. R.; Colarossi, F. E.; Lynch, G. S. Notexin Causes Greater Myotoxic Damage and Slower Functional Repair in Mouse Skeletal Muscles than Bupivacaine. *Muscle Nerve* 2006, *34*, 577−585

44. Takekura, H.; Fujinami, N.; Nishizawa, T.; Ogasawara, H.; Kasuga, N. Eccentric Exercise-induced Morphological Changes in the Membrane Systems Involved in Excitation_Contraction Coupling in Rat Skeletal Muscle. *J. Physiol.* 2001, *533*, 571−583.

46. CONNOLLY, D. A. J.; SAYERS, S. E.; MCHUGH, M. P. Treatment and Prevention of Delayed Onset Muscle Soreness. *Journal of Strength and Conditioning Research* 2003, *17* (1), 197–208.

47. Rantanen, J.; Thorsson, O.; Wollmer, P.; Hurme, T.; Kalimo, H. Effects of Therapeutic Ultrasound on the Regeneration of Skeletal Myofibers after Experimental Muscle Injury. *The American Journal of Sports Medicine* 1999, *27*, 54–59.

48. Sarver, D. C.; Sugg, K. B.; Disser, N. P.; Enselman, E. R. S.; Awan, T. M.; Mendias, C. L. Local Cryotherapy Minimally Impacts the Metabolome and Transcriptome of Human Skeletal Muscle. *Scientific Reports* 2017, *7* (1).

Applicant

Niranjan Chatterjee